Korean J. Chem. Eng., 39(11), 2883-2895 (2022)
DOI: 10.1007/s11814-022-1276-z

pISSN: 0256-1115
eISSN: 1975-7220

INVITED REVIEW PAPER

A review of formic acid decomposition routes on transition metals for its potential use as a liquid H_2 carrier

Sierra Schlussel and Stephanie Kwon†

Department of Chemical and Biological Engineering, Colorado School of Mines, Golden, Colorado 80401, United States
(*Received 27 June 2022 • Revised 11 August 2022 • Accepted 28 August 2022*)

Abstract−Formic acid (HCOOH) has emerged as a promising H_2 energy carrier due to its reasonable gravimetric and volumetric H_2 densities, low toxicity, low flammability, and ease of handling. Its possible productions from biogenic feedstocks also make it an attractive source to produce H_2 on demand. The utilization of HCOOH as a liquid H_2 carrier requires catalytic systems to selectively dehydrogenate HCOOH at low temperatures without forming CO products that can act as a poison in fuel cell applications. In this review, we summarize the recent progress in understanding HCOOH decomposition via dehydrogenation (to CO_2/H_2) and dehydration (to CO/H_2O) pathways on transition metals, including Cu, Pt, Pd, and Au. The focus is on discussing the surface chemistry of HCOOH reactions on transition metals, including the types of bound intermediates and the identity and kinetic relevance of elementary steps. In doing so, we review current catalyst design strategies for HCOOH dehydrogenation to facilitate the future development of catalytic processes for H_2 storage/utilization.

Keywords: Catalytic Dehydrogenation, Hydrogen Storage, Formic Acid, Transition Metals, Density Functional Theory

INTRODUCTION

The production of green hydrogen (H_2) via low-temperature H_2O electrolysis has emerged as a strategy to combat the current environmental and energy crisis due to its high energy density (120 MJ/kg), availability, and clean nature [1]. The successful implementation of an H_2 economy relies on the development of energy- and cost-effective technologies to adequately store and transport H_2, especially for its use in distant and remote locations. Currently, liquid H_2 is the most used form in prototype automobiles because of its high H_2 density (70 kg H_2/m^3 at standard temperature-pressure (STP); Table 1) [2]. However, such a "tank method" suffers from the high energy demand required to achieve cryogenic conditions for liquefication [3]. Alternative approaches, such as H_2 adsorption on high surface area materials (e.g., carbon nanotubes [4] and metal organic frameworks (MOFs) [5]), have shown limited success due to low gravimetric (<2.3 H_2 % wt.) and volumetric density (<14.7 kg H_2/m^3) at ambient temperatures (~298 K); the best Cu-MOFs have achieved high gravimetric and volumetric density (9.95 H_2 % wt.; 53 kg H_2/m^3) but only at very low temperatures (~77 K) and both capacities decreased significantly at higher operating temperatures (~298 K) [5-7]. More recently, hydrogenation/dehydrogenation reactions have emerged as a technology to store and release H_2 on-demand (Table 1). Examples of liquid H_2 carriers include methanol, methyl cyclohexane, cyclohexane, and formic acid, all of which benefit from easy transportation and long-term storage without requiring cryogenic devices, high-pressure systems, or gas-pipe lines [8,9].

Among liquid H_2 carriers, formic acid (HCOOH) has emerged

Table 1. Summary of physical and chemical properties of potential H_2 carriers

H_2 carrier	Boiling point (K)	Density (kg/m^3)[a]	Gravimetric content (H_2 % wt.)	Volumetric content (kg H_2/m^3)[b]	Flash point (K)	Ref.
Liquid H_2	20.3	71	100	70	-	[2]
Methanol	337.8	790	12.1	100	284	[2,10,12]
Ammonia	239.8	730	17.8	121	405	[2,10,13,14]
Methyl cyclohexane	373.6	770	6.2	47	269	[2,10,13]
Cyclohexane	353.9	780	7.2	56	253	[2,10]
Formic acid	373.9	1,220	4.4	53	342	[2,10]

[a]At standard temperature-pressure (STP) conditions.
[b]Calculated from the density of respective molecules at STP.

†To whom correspondence should be addressed.
E-mail: kwon@mines.edu

as one of the most promising chemicals due to its relatively high H_2 density (4.4 H_2 % wt.; 53 kg H_2/m^3; Table 1), low toxicity, environmentally benign nature, low flammability, and ease of handling. HCOOH has a high boiling point (373.9 K [10]) and thus remains as a liquid under a wider range of temperatures; the current existing gasoline infrastructure thus could potentially be adapted for HCOOH distribution. Cyclohexane and methyl cyclohexane exhibit higher gravimetric H_2 density than HCOOH (4.4 vs. 7.2 and 6.2 H_2 % wt.; Table 1) but are highly flammable, as indicated by their lower flash points compared to HCOOH (342 vs. 253 and 269 K; Table 1), rendering them unattractive H_2 carriers, especially in the transport sector. Benzene, the dehydrogenated product of cyclohexane, is carcinogenic, raising significant health concerns on the use of the cyclohexane-benzene cycle for H_2 storage. Although the gravimetric H_2 density of HCOOH (4.4 H_2 % wt.) is lower than the goal set by the U.S. Department of Energy (5.5 H_2 % wt.), its high density (1,220 kg m^{-3} at STP) results in a high volumetric H_2 content (53 kg H_2 m^{-3}), equivalent to the energy density of 1,770 kWh m^{-3}, exceeding the current industrial standard (i.e., the Toyota Mirai 70 MPa H_2 storage tank with 1,400 kWh m^{-3}) [11].

HCOOH decomposition can occur via dehydrogenation or dehydration pathway [15]:

$$HCOOH(g) \rightarrow CO_2(g) + H_2(g) \quad (\Delta G_{298\,K} = -48.4\ kJ\ mol^{-1}) \quad (1)$$

$$HCOOH(g) \rightarrow CO(g) + H_2O(g) \quad (\Delta G_{298\,K} = -28.5\ kJ\ mol^{-1}) \quad (2)$$

H_2 production via HCOOH decomposition thus forms a stoichiometric amount of CO_2. However, HCOOH synthesis (from CO_2/H_2; the reverse of Eq. (1)) also uses a stoichiometric amount of CO_2, and thus the overall cycle can be carbon neutral, especially when the CO_2 recycling and HCOOH formation steps are efficient; more detailed discussion can be found in the previous review by Ahn et al. [16]. The selectivity between dehydrogenation and dehydration pathways (Eqs. (1) and (2)) depends sensitively on the type and nature of the catalysts and operating conditions. The successful utilization of HCOOH as a potential H_2-carrier thus requires the development of active, selective, and stable catalysts that can release H_2 on demand at low temperatures without the formation of CO products, which can limit the use of H_2 product stream in applications using noble metals due to CO poisoning; for example, a fuel cell uses Pt electrodes that are significantly inhibited even with the presence of 10 ppm-level of CO [17].

In this review, we summarize the recent progress in understanding HCOOH dehydrogenation and dehydration pathways on transition metals (Cu, Pd, Pt, Au) that are widely used as active metals for the reaction. We only discuss thermo-catalytic reactions; electrochemical oxidation of HCOOH [18-21], which constitutes a substantial body of literature, falls outside the scope of this review. We focus on the surface chemistry involved in these reactions with the goal of providing insight into the catalytic properties that influence their reactivity and selectivity. We also briefly review catalyst design strategies for HCOOH dehydrogenation and ultimately aim to facilitate the future development of catalytic processes for H_2 storage and utilization.

HCOOH DECOMPOSITION PATHWAYS ON TRANSITION METALS

HCOOH reactions on metals and oxides were widely studied in the '70-'80s, as simple probe reactions to understand the surface properties of a variety of catalysts. HCOOH reactions can involve formate (HCOO*) or carboxylate (COOH*) intermediates, formed via activating O-H or C-H bonds in HCOOH (Fig. 1). Formates can present either in the bidentate configuration on two vicinal metal atoms ($HCOO_B$*) or in the monodentate configuration on one metal atom ($HCOO_M$*) [22,23]. Both HCOO* intermediates can lead to

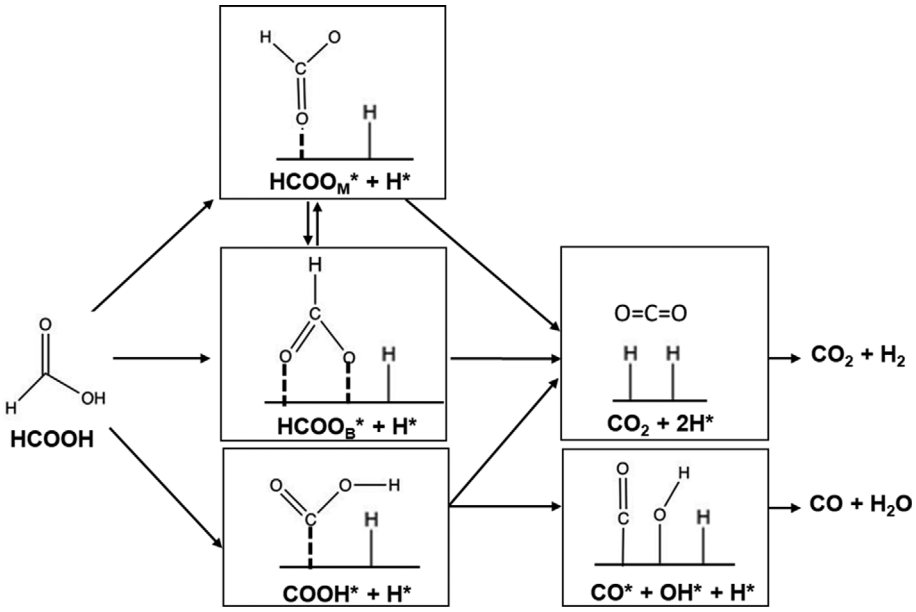

Fig. 1. Schematic of HCOOH decomposition pathways on transition metal surfaces, based on the proposed mechanisms discussed in reference [23].

the formation of CO_2 products via a subsequent C-H activation in HCOO*, where the resulting H-atoms (H*) are released as H_2(g) via a re-combinative H_2 desorption (Fig. 1). The alternative COOH* intermediate can lead to the CO_2 product as it cleaves its O-H bond or to the CO product by activating its C-O bond; in the latter case, OH* recombines with H* to form H_2O (Fig. 1). The relative contributions of HCOO* and COOH* pathways and CO_2/CO selectivity depend on the identity and the nature of the catalysts. Here, we review the surface chemistries of HCOOH dehydrogenation (to CO_2/H_2) and dehydration (to CO/H_2O) pathways on the most common transition metals (Cu, Pt, Pd, Au) and their surface properties that determine their rates and selectivity, by summarizing literature based on experimental and computational studies.

1. Copper (Cu)

HCOOH reactions have been extensively studied on Cu catalysts [24-34]. Only dehydrogenation products (CO_2/H_2) are reported on single crystal Cu surfaces [24-28,30,31] and Cu nanoparticles (dispersed on SiO_2 [35,36] and Al_2O_3 [32,36] supports) without any detectable formation of dehydration products (CO/H_2O). HCOOH dehydrogenation on Cu catalysts is suggested to proceed via a $HCOO_B$* pathway, evidenced by spectroscopic studies that detected $HCOO_B$* species upon HCOOH exposure on Cu(110) and Cu(100) surfaces [24,25,29]. Transient studies found that these $HCOO_B$* species are formed on Cu(110) even at 200 K, where H* formed upon $HCOO_B$* formation recombine and desorb as H_2(g) below ambient temperature [27]. The stranded $HCOO_B$* on Cu(110) decomposes at higher temperatures (~460 K) to form CO_2(g) and H_2(g). The decomposition rates are limited by the C-H activation in $HCOO_B$*, as indicated by the CO_2/H_2 (or CO_2/D_2) evolution profiles that are shifted to higher temperatures for $DCOO_B$* than those for $HCOO_B$* (k_{HCOO*}/k_{DCOO*}~2.9±0.7) [30,31]. These mechanistic conclusions from experiments are consistent with theoretical studies based on density functional theory (DFT) calculations conducted by Li et al., who showed that $HCOO_B$* pathways are preferred over COOH* pathways on Cu(111), Cu(100), and Cu(211) surfaces [32].

The structure-sensitivity of HCOOH dehydrogenation on Cu catalysts has remained controversial in literature. Iglesia and Boudart suggested that the reaction is structure insensitive, supported by measured activation barriers that remained essentially the same as the fractional Cu dispersion was varied from 0.001 to 0.2 (Fig. 2). This study also showed that the reactivity of bound $HCOO_B$* species on Cu does not depend on the identity of supports, indicated by similar dehydrogenation turnover rates and activation energies measured on Cu/SiO_2, Cu/Al_2O_3, and bulk Cu powders [34]. In contrast, Li et al. suggested that HCOOH dehydrogenation catalysis is strongly surface sensitive; their DFT calculations demonstrated that the activation barriers for the $HCOO_B$* decomposition (i.e., the energy of the C-H activation transition state (TS) referenced to the $HCOO_B$* precursor) increase in the order of Cu(111)<Cu(100)< Cu(211) (92, 117, and 142 kJ/mol, respectively) (Fig. 3), due to the strong binding of $HCOO_B$* species on under-coordinated sites [32]. These results led the authors to conclude that these under-coordinated steps, corners, or defect sites could be mostly covered by strongly bound $HCOO_B$* intermediates and that HCOOH decomposition would occur mostly on the terrace sites of Cu nanoparticles. This may explain observed surface-insensitivity during steady-state catalysis.

In contrast to the unimolecular $HCOO_B$* decomposition pathway suggested by previous DFT calculations (at low surface coverage limits) [32] and surface science studies performed under ultra-high vacuum environments [30-32], Iglesia and Boudart proposed the involvement of a bimolecular $HCOO_B$* decomposition pathway during steady-state catalysis (when gas-phase HCOOH reactants co-exist with $HCOO_B$*) [34]. This proposal was based on their observations, where activation barriers were lower when measured during steady-state catalysis than during transient decomposition of bound $HCOO_B$* species (97 vs. 133 kJ mol^{-1}) [34]. In line with these findings, DFT results by Chen et al. demonstrated that the formation of bimolecular H-bonded complex formed between molecularly bound HCOOH and $HCOO_B$* facilitates the decom-

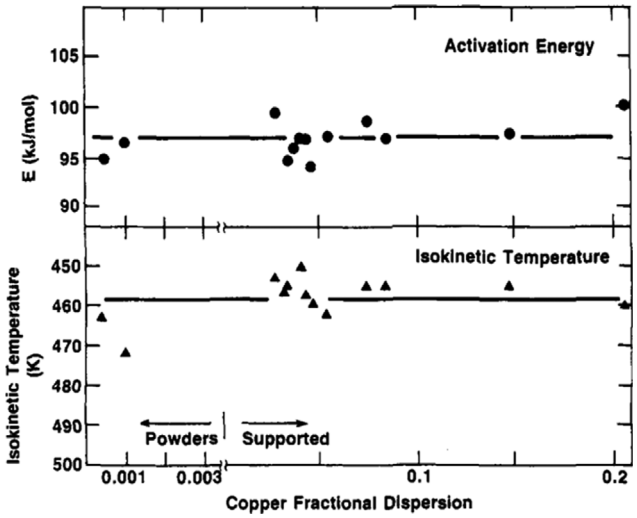

Fig. 2. Effects of Cu dispersion on isokinetic temperature (the temperature required to achieve 0.16 s^{-1} decomposition rate) and activation energy for HCOOH decomposition (Reproduced with permission from Ref. [34], Copyright 1986, American Chemical Society).

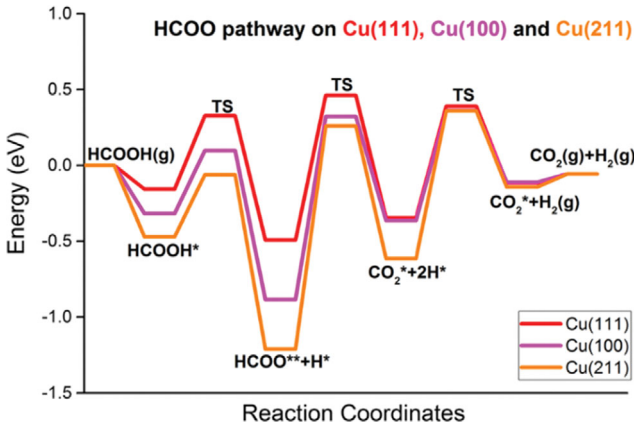

Fig. 3. DFT-derived electronic energy (eV) of intermediates and TSs involved in HCOOH dehydrogenation catalysis on Cu(111), Cu(100), and Cu(211) surfaces (Reproduced with permission from Ref. [32], Copyright 1994, Springer New York).

position of $HCOO_B$* species [33]. More recently, Lin et al. further provided spectroscopic evidence that supports the existence of the HCOOH-$HCOO_B$* complex during HCOOH dehydrogenation on Cu/SiO_2 [35]. Antisymmetric bands for $HCOO_B$* species became stronger upon H-bonding with vicinal HCOOH because such an H-bonding perturbs the induced dipole moment of $HCOO_B$* upon vibration, consistent with DFT-derived vibrational frequency and intensity for the HCOOH-$HCOO_B$* species. DFT-derived activation barriers and those determined from CO_2 evolution rates from pre-adsorbed $HCOO_B$* species are about 10 kJ mol^{-1} smaller in the presence of HCOOH(g) than those for the unimolecular decomposition of bound $HCOO_B$* species, reflecting that vicinal HCOOH may stabilize the C-H activation TS of $HCOO_B$* decomposition preferentially relative to its $HCOO_B$* precursor. These works, in turn, show how the reaction mechanisms during practical catalysis may be different from those expected from surface science studies conducted in ultra-high vacuum or inert environments and computational studies performed at clean surface limits due to the high coverages of reactant derived species.

2. Platinum (Pt)

Pt has been suggested as the most active metal for HCOOH dehydrogenation catalysis among the common transition metals examined (Au, Pt, Ag, Pd, Cu, Ni, Co, Rh), evidenced by the pre-adsorbed formates on Pt that decomposed at the lowest temperature during temperature-programmed decomposition (TPD) analysis (Fig. 4). Such a trend correlated well with the turnover rates measured on these metal catalysts during steady-state analysis [37].

Analogous to the HCOOH dehydrogenation mechanism on Cu, $HCOO_B$* has been widely suggested as the most abundant surface intermediates (MASI) on Pt surfaces. Tang et al. detected only $HCOO_B$* (but not COOH*) on metallic Pt powders from their infrared spectra, suggesting $HCOO_B$* as the sole HCOOH-derived intermediates [37]. Jensen et al. also observed formates during HCOOH reactions on Pt(111) using low-energy electron diffraction (LEED) and electron stimulated desorption ion angular distribution (ESDIAD) techniques, where formates decomposed to form

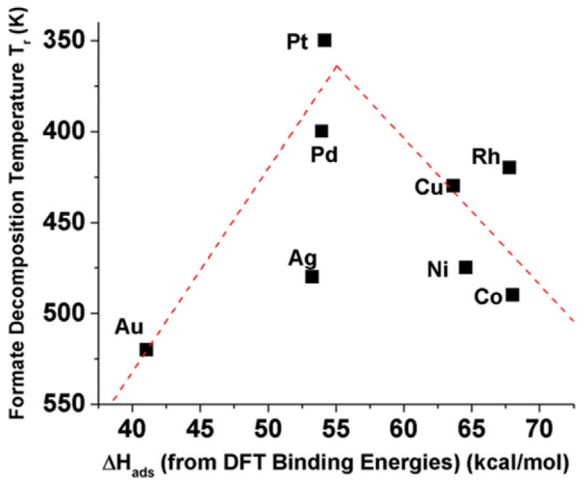

Fig. 4. Decomposition temperature (T_r(K)) of adsorbed formates on metallic powders from TPD measurements as a function of formate binding energy on metal (111) surfaces from DFT methods (Reproduced with permission from Ref. [37], Copyright 1962, Elsevier).

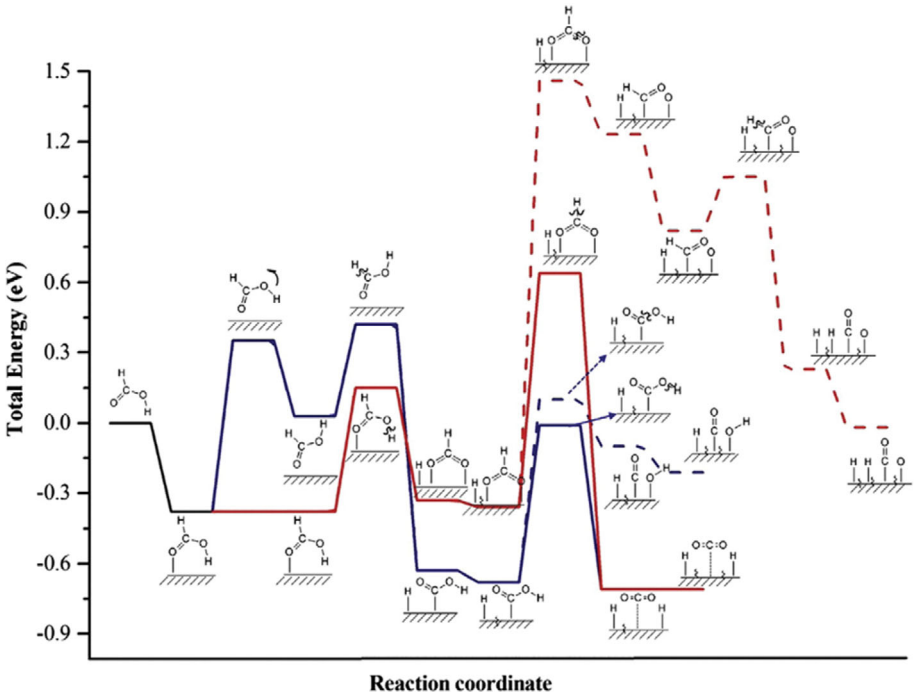

Fig. 5. DFT-derived energy (eV; electronic energy without any corrections) of intermediates and TSs involved in HCOOH decomposition on Pt(111); the energies of the clean Pt(111) surface and HCOOH(g) are taken as a reference (Reproduced with permission from Ref. [41], Copyright 1964, Elsevier).

CO_2/H_2 products at ~260 K [38]. Similar conclusions were made by Avery, who used electron energy loss spectroscopy (EELS) to show that HCOOH binds on clean and O*-covered Pt(111) to form $HCOO_B$* species that decomposed exclusively to form CO_2 products at ~260 K [39]. Abbas and Madix also agreed with the formate pathway based on their TPD analysis, where CO_2 evolved from deuterated formates ($DCOO_B$*) on Pt(111) at ~265 K [40].

More recently, theoretical studies based on DFT methods suggest the possible involvement of COOH* intermediates during HCOOH reactions on Pt catalysts. Scaranto et al. showed, based on their DFT calculations, that COOH* species, formed via a C-H activation in molecularly bound HCOOH*, are the most stable HCOOH-derived intermediates on Pt(111) (Fig. 5) [41]; such a conclusion is supported by numerous other theoretical studies [23,41,42]. This C-H activation step (that forms COOH*) imposes the highest barrier along the COOH*-pathway, and the subsequent O-H activation in COOH* forms a CO_2 product with a much smaller barrier. This DFT study also demonstrated that COOH* species can lead to the formation of CO via C-O bond activation in COOH*. Yet, such a dehydration route requires a higher barrier than the dehydrogenation route (75 vs. 65 kJ/mol, referenced to the COOH* precursor), explaining the higher selectivity towards CO_2 products on Pt catalysts [41]. These *COOH* routes based on theoretical calculations, however, are inconsistent with infrared studies that detected only $HCOO_B$* during HCOOH reactions on single crystal Pt surfaces [39] and Pt powders [37].

It has been suggested that HCOOH selectively dehydrogenates on Pt surfaces to form CO_2/H_2 products; only CO_2/H_2 products are reported on supported Pt nanoparticles (Pt/Al_2O_3) [43] and on Pt(111) [44]. Some studies, in contrast, detected CO products, which are suggested to be predominantly formed at defect sites [40]. For example, Avery observed CO desorption (at ~470 K) during transient TPSR measurements and suggested that such CO products are formed at defect sites within the Pt(111) samples (e.g., Pt support or edge/back of the Pt(111) crystals), evidenced by the lack of CO signals on the "well-defined part" of the Pt(111) surface during the EELS experiments [39]. Abbas and Madix also detected both CO and CO_2 products from DCOOH reactions on Pt(111) and suggested that CO molecules are mainly formed at the defect sites within Pt surfaces (that account for nearly ~10% of the total sites), evidenced by CO formation that can be fully suppressed by preferential sulfur adsorption on such sites.

Even a very small amount of CO, irrespective of provenance, can drastically impact reaction rates and HCOOH decomposition routes by covering a significant portion of the surfaces; for example, near-saturation CO* coverage can be achieved even at 125 ppm CO on Pt/SiO_2 (363 K) [45]. Columbia et al. showed in their ultrahigh vacuum studies that the presence of CO* (>0.4 ML) completely quenched CO_2/H_2 formation from HCOOH by blocking sites for HCOOH adsorption and formate formations, when CO was intentionally co-fed to the system along with HCOOH reactants [46]. Bhandari et al. showed, based on microkinetic modeling and DFT-derived reaction energy and activation barrier, that Pt(111) surfaces would be nearly saturated with CO* (>0.9 ML) during HCOOH catalysis, where CO molecules are formed as minor products upon HCOOH decomposition [47]. This theoretical study demonstrated that on Pt surfaces partially covered with CO* (0.44 ML), HCOOH dehydrogenation occurs via a COOH* intermediate, where the spectator CO* acts as a co-catalyst, abstracting H-atom from COOH* to form CO_2. These studies, in turn, demonstrate how the surface coverage of intermediates but also spectators (CO*) can significantly influence reaction pathways, requiring a detailed understanding of surface coverage during catalytic turnovers to provide molecular-level pictures of reactions relevant in realistic conditions.

3. Palladium (Pd)

Over the last decade, Pd-based catalysts have received increasing interest for HCOOH dehydrogenation due to their high reactivity at near ambient temperature [37,48-63]. The types of reactive intermediates and the identity of elementary steps involved in HCOOH reactions on Pd surfaces, however, have remained unclear in literature. Jorgensen and Madix showed from their EELS experiments that, at 80 K, HCOOH binds molecularly on clean Pd(100) surfaces; bound formate species were not detected as the sample was heated to 170 K. Instead, these molecularly bound HCOOH species partially desorbed as HCOOH(g), and the remaining surface-bound HCOOH led to the formation of CO products, which desorbed at ~515 K, without any detectable formation of CO_2 [54]. In contrast, monodentate formates were readily formed on O*-covered Pd(100) upon the introduction of HCOOH at 80 K; during TPD analysis of pre-adsorbed HCOOH on O*-covered Pd(100), H_2O evolved at ~170 K, supporting that the proton transfer to O* upon the $HCOO_M$* formation. $HCOO_M$* species on Pd(100) decomposed to form CO_2 products at ~265 K, with the rate limited by the C-H activation in formates. H_2 evolution occurred at ~340 K, with the rates limited by the desorption step. The authors also discussed that a significant amount of CO was evolved at 515 K, specifically when the initial O* coverage was <0.1 ML with the saturation dosage of HCOOH.

In contrast to Pd(100) surfaces that require O* for formate formations, Davis and Barteau reported that HCOOH molecules dissociate to form formates on clean Pd(111) at ~200 K [55]. Formate species on Pd(111) decompose at higher temperature, leading to the evolution of CO_2 (~260 K), H_2 (~330 K), and CO (~490 K) with a CO_2/CO selectivity of 1.6. With the presence of O*-layers on Pd(111), formates decomposed to form CO_2 at ~280 K, which was 20 K higher than on clean Pd(111), with a smaller amount of CO formed upon formate decomposition (CO_2/CO=15.5). Also, more than half of the O*-layers on Pd(111) were consumed upon HCOOH adsorption and desorbed as H_2O~170 K, again suggesting that the role of O* as Brønsted base that upon the formate formation. These results from ultrahigh vacuum studies suggest the possible role of O* in HCOOH reactions on Pd surfaces, although it has remained unclear why the O* layers dramatically change the CO_2/CO selectivity and how these reaction pathways with O*-covered surfaces would be relevant during steady-state catalysis.

Previous DFT calculations on Pd(111) and Pd(100) surfaces at low surface coverage limits (≤1/9 ML) suggested that HCOOH dehydrogenation can proceed via both $HCOO_B$* and COOH* intermediates, where only the latter can also lead to the formation of CO products (Fig. 6) [56-58]. This mechanistic conclusion from theoretical results on "clean" Pd surfaces, however, contradicts spectroscopic studies that observed only formate species on Pd surfaces

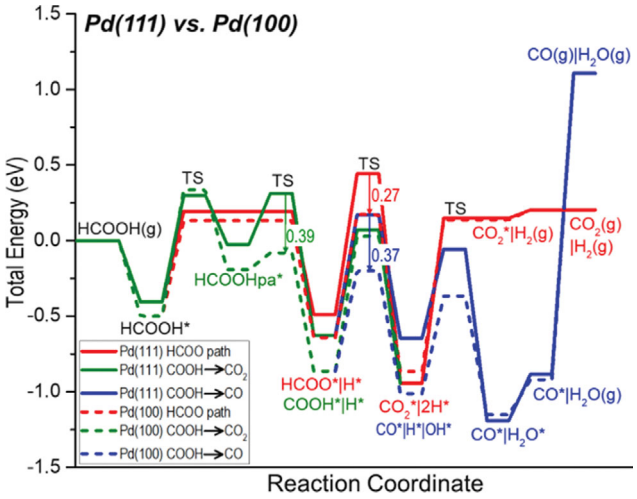

Fig. 6. DFT-derived energy (in eV) of reactive intermediates and TSs involved in HCOO* and COOH* pathways on Pd(100) (solid lines) and Pd(111) (dashed lines) surfaces. The arrows show the downshift in TS energy on Pd(100) compared to Pd(111) (Reproduced with permission from Ref. [58], Copyright 1964, Elsevier).

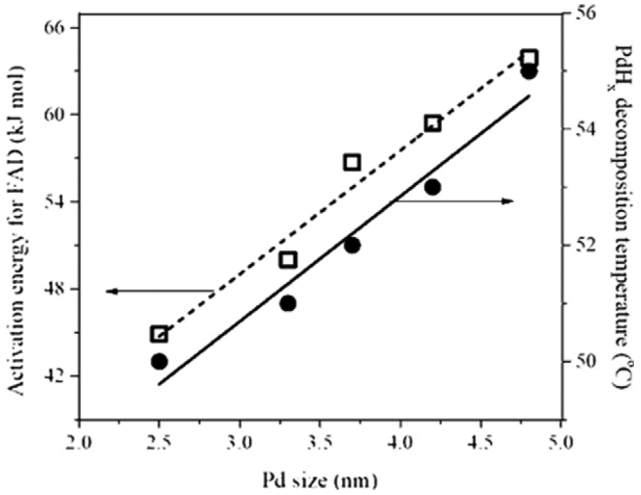

Fig. 7. Apparent activation energy of HCOOH dehydrogenation (1 M HCOOH in H_2O; 303-333 K) on Pd/C (left axis) and the decomposition temperature of PdH_x, measured from temperature-programmed decomposition (TPD) analysis after reduction of Pd/C at 373 K in H_2 (the right axis) as a function of average Pd sizes (from TEM images) (Reproduced with permission from Ref. [64], Copyright 1992, Elsevier).

[37,54]. This discrepancy may indicate the presence of co-adsorbed species that can impact the reaction route and the stability of bound species. For example, Davis and Barteau showed that CO* and O* species co-exist with formates on Pd(111) surfaces upon HCOOH reactions based on their vibrational spectra [55]. A recent theoretical work by Li et al. reported that the presence of 0.55 CO* ML renders the $HCOO_B$* pathway significantly unfavorable on both Pd(100) and Pd(111) surfaces [58]. HCOOH reactions rather proceed via a COOH* intermediate, which preferentially decomposes to CO on Pd(111) and to CO_2 on Pd(100), indicating a significant structure dependency on reaction selectivity. The co-adsorbed H_2O can also play an important role, especially during HCOOH reactions in aqueous solutions [59]. For example, DFT calculations by Zhang et al. showed that the H-bonding between the H_2O and the reactive intermediates and TSs leads the reaction to prefer the $HCOO_B$* pathway in the presence of co-adsorbed H_2O [57].

Most of the recent reaction studies with Pd catalysts, in fact, were performed in aqueous solutions at low temperatures (<333 K) [48-53]; sodium formate is often added to the solution as an additive to increase the reaction rates by increasing formate concentrations [60-62]. In aqueous solutions, HCOOH reactions on supported Pd catalysts (Pd/C) did not yield any CO at a detectable level (<10 ppm), rendering it an attractive catalyst option for HCOOH dehydrogenation catalysis at near ambient temperatures [49]. Assessing reaction mechanisms in liquid-phase catalysis is more challenging due to the possible involvements of solvent effects, active site leaching, and mass transfer limitations. Kim et al. combined kinetic and theoretical methods to suggest that re-combinative H_2 desorption is a kinetically relevant step during HCOOH dehydrogenation on Pd/C catalysts in a liquid-phase [48]. This mechanistic conclusion was based on a large barrier for H_2 desorption in DFT calculations and observed strong kinetic isotope effects (KIE) for DCOOH (+H_2O) and weaker effects for HCOOD (measured with HCOOH+D_2O). Yet, it has remained unclear why KIE for the C-H substitution (HCOOH vs. DCOOH) are much stronger than that for the O-H substitution (HCOOH vs. HCOOD), when the similar effects are expected if the H_2 re-combinative desorption is the kinetically relevant step. Reported DFT calculated energy also did not include entropic effects, making it difficult to compare reaction steps that involve very different entropy.

Several works have reported the particle size effects of Pd nanoparticles on HCOOH dehydrogenation rate where rates increased with decreasing Pd particle size. Kim et al. showed that apparent activation energy for HCOOH dehydrogenation on Pd/C catalysts scale almost linearly with the average Pd sizes (estimated from TEM images), leading to higher rates for the smaller Pd particles (Fig. 7). They attributed this trend to the more difficult H_2 desorption from larger clusters, as indicated by the TPD profiles of size controlled Pd/C catalysts after their reduction at 373 K (Fig. 7) [64]. Li et al. also reported a similar trend, where the catalytic rates increased by a factor of 3.6 as the particle size decreased from 4.5±0.5 to 2.1±0.3 nm (estimated from scanning transmission electron microscopy, STEM) [58]. The authors suggested that much higher rates of smaller Pd particles originate from the higher Pd dispersion and the presence of a larger proportion of Pd with positive charges (instead of metallic Pd), based on their ex-situ X-ray photoelectron spectroscopy (XPS) measurements. More research would be needed to further understand how the electronic state of Pd influences reaction routes and how such electronic states change under reaction conditions.

The stability of Pd catalysts during HCOOH reactions in aqueous solutions, which has been discussed in literature [51,52,63], is an important factor in their use in industrial applications. Kim et al. showed that supported Pd catalysts completely deactivated after the third use (a third injection of formic acid reactants into the liq-

uid-phase solvent with Pd/NH_2-C catalysts) without the regeneration process involving washing and drying in between runs, which could be attributed to the deposition of reactant/product-derived species on Pd surfaces [51]. Early work by Ruthven and Upadhye suggested that the deactivation of Pd black catalysts during HCOOH decomposition in an aqueous solution is caused by the accumulation of H* on Pd surfaces, based on their kinetic analysis [63]. Hu et al. showed that the reactivity of Pd/C catalysts can be fully recovered by drying the used catalysts at 383 K, which led the authors to suggest that the deactivation is not caused by the agglomeration or loss of Pd active sites in the solution [52]. They performed TPD analysis on used catalysts with online mass-spectrometer to show the absence of CO evolution, indicating that CO* was not the source of deactivation. Instead, they observed H_2/CO_2 evolution, from which they proposed that the deactivation is caused by the formation of HCOO* species on Pd surfaces that cannot be decomposed at low operating temperature, although whether it is HCOO* or COOH* species cannot be verified without spectroscopic evidence.

Recent works have focused on utilizing Pd-based bimetallic systems for HCOOH dehydrogenation catalysis (e.g., Pd-Au [65,66], Pd-Ag [65,67,68]), which were suggested to improve both reactivity and stability of Pd catalysts during liquid-phase HCOOH reactions. Zhou et al. compared monometallic Pd with bimetallic Pd-Cu, Pd-Ag, and Pd-Au nanoparticles (supported on C) for HCOOH dehydrogenation catalysis [65]. In doing so, they showed that the reactivities of Pd-Au/C and Pd-Ag/C were stable while Pd/C catalysts deactivated within the first few minutes; they attributed this result to a retention of the reduced state of Pd in the bimetallic system versus the monometallic system. The authors suggested that Pd-Au/C showed the highest activity when compared per g-metal basis; although it is difficult to directly compare their performance due to the lack of information about the surface dispersion of these bimetallic systems and the exposed number of each metal component. Zhang and coworkers also showed the enhancement effects of Ag on the catalytic reactivity of Pd by forming bimetallic systems with the reactivity following the volcano plot as the Ag content increased in the Ag-Pd catalysts (Fig. 8) [67]. Further research would be required to understand how the presence of second metals influences the reaction pathways and the stability of bound intermediates and TSs, governing the reaction rates, selectivity, and stability.

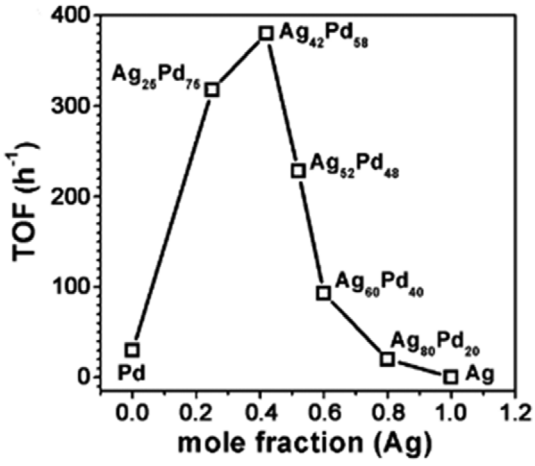

Fig. 8. Turnover frequency (TOF) as a function of a mole fraction of Ag in Ag_xPd_y bimetallic catalysts (1 M HCOOH in H_2O; 323 K) (Reproduced with permission from Ref. [67], Copyright 2013, John Wiley and Sons).

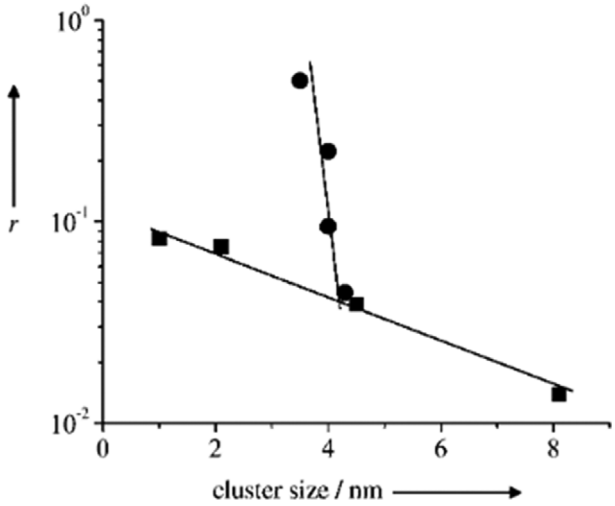

Fig. 9. HCOOH dehydrogenation turnover rate (mol s^{-1} g-at $metal_s^{-1}$) on Au/Al_2O_3 (●; 2 kPa HCOOH) and Pt/Al_2O_3 (■; 4 kPa HCOOH) at 353 K as a function of average metal cluster size estimated from TEM images (Reproduced with permission from Ref. [43], Copyright 2009, John Wiley and Sons).

4. Gold (Au)

Au had not been considered an active metal for HCOOH dehydrogenation catalysis (Fig. 4), until Ojeda and Iglesia reported that highly dispersed Au nanoparticles (on Al_2O_3 support) can dehydrogenate HCOOH at nearly ambient temperature (~350 K) without forming any CO at a detectable level (<10 ppm CO) [43]. Measured HCOOH dehydrogenation turnover rates (per surface metal) on Au/Al_2O_3 were an order of magnitude higher than those on Pt/Al_2O_3, specifically when Au presented as very small nanoparticles (<4 nm; Fig. 9). The authors suggested that the active sites, in fact, reside at the surfaces of the TEM-invisible clusters, evidenced by the turnover rates that dramatically decreased within high temperature O_2 treatment without noticeable change in the average size of Au clusters in the TEM images. The catalytic performance (e.g., activity and selectivity) of Au catalysts, indeed, depends strongly on the identity of the supports, as shown by Gazsi et al. (Fig. 10), which suggests that the size distribution of Au nanoparticles differs significantly across different types of supports and that the possible role of oxide supports in dehydrating HCOOH at higher temperatures (forming unwanted CO products) [69]. Consistently, Singh et al. also showed that measured HCOOH dehydrogenation rates are a strong function of the size of Au clusters, with rates that increased two orders of magnitude as the size of Au nanoparticles (determined by STEM images) decreased from 10.7 to 2.6 nm [70].

DFT calculations (PW91 functionals) on Au(111), Au(100), and Au(211) surfaces showed that the $HCOO_B$*-mediated pathway is preferred on Au(100) and Au(211) surfaces, while both $HCOO_B$* and COOH* pathways are plausible on Au(111) [70]. Yet, DFT-derived energy of intermediates and TSs on these surfaces are much

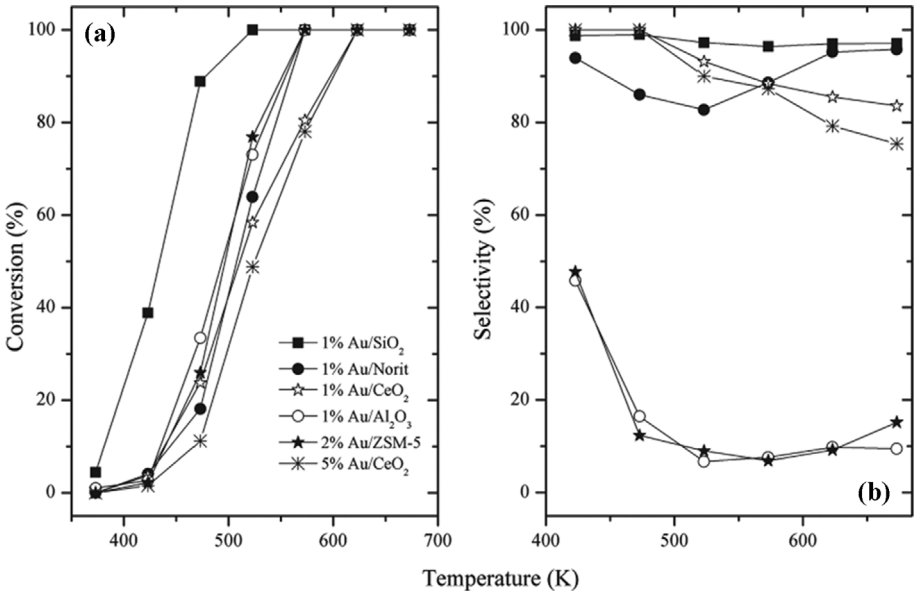

Fig. 10. HCOOH (a) conversion and (b) selectivity on supported Au catalysts as a function of temperatures (Reproduced with permission from Ref. [69], Copyright 2011, American Chemical Society).

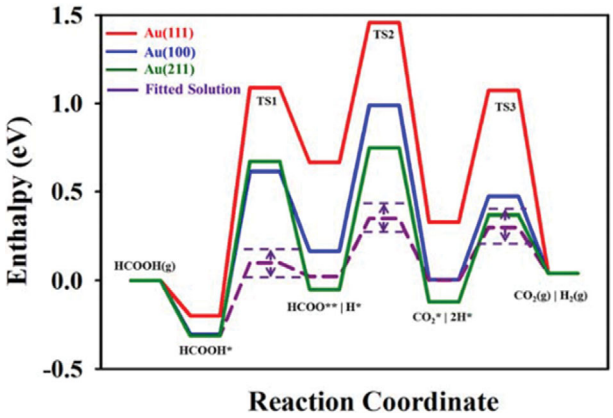

Fig. 11. DFT-derived enthalpy (in eV) of intermediates and TSs involved in HCOOH dehydrogenation via HCOO* intermediates on Au(111), Au(110), and Au(211) surfaces. The purple dashed lines show the "best-fitted solution" (along with the confidence intervals) obtained by adjusting the binding energy of all intermediates and TS energy to reach the agreement between the model predicted reaction rates and the experimental values (Reproduced with permission from Ref. [70], Copyright 2014, John Wiley and Sons).

less favorable than those expected from experiments (Fig. 11); the "best-fitted solutions" are shown in Fig. 11, which are obtained by adjusting the binding energy of all intermediates and TS energy to reach the agreement between the model predicted reaction rates and the experimental values. These discrepancies led the authors to conclude that i) Au(111), Au(100), and Au(211) surfaces cannot accurately represent the active sites for HCOOH dehydrogenation catalysis, and ii) the active sites in Au clusters might be more undercoordinated than these facets investigated. These authors also showed from the degree of rate control analysis for the "best-fitted solutions" that the C-H activation of $HCOO_B$* on Au clusters controls the overall turnover rates, analogous to unimolecular HCOOH dehydrogenation on Cu surfaces (discussed in Section 2.1).

Ojeda and Iglesia discussed, based on their kinetic analysis, that the mechanism of HCOOH dehydrogenation on "TEM-invisible" Au clusters may be different from the conventional unimolecular HCOOH dehydrogenation [43]. They observed normal KIE for both C-H and O-H activations, although the impact of deuterium substitution in the O-H bond was weaker than that in the C-H bond (r_{HCOOH}/r_{DCOOH}=2.5; r_{HCOOH}/r_{HCOOD}=1.6; 2 kPa HCOOH; 353 K). Notably, only HD isotopomer was detected from HCOOD or DCOOH reactions on Au clusters without any formation of H_2 and D_2. This result led the authors to suggest the irreversible formation of H_2 exclusively from the reaction between the H-atom in the OH group and the H-atom in the C-H group in HCOOH. The authors concluded that HCOOH forms a formate intermediate via a quasi-equilibrated OH activation step. This formate decomposes via a reaction with the H-atom (formed upon the formate formation from HCOOH), where this H-assisted C-H activation step kinetically controls the overall rates, as suggested by the measured KIE values and the exclusive evolution of HD.

More recent theoretical calculations by Chen et al. disagreed with this H-assisted C-H activation pathway [71]. Based on their kinetic Monte Carlo simulations along with DFT calculations, they showed that HCOOH dehydrogenation on Au_{18} clusters (~0.8 nm) occurs via a $HCOO_B$* pathway with the C-H activation in $HCOO_B$* kinetically controlling the overall rates (Fig. 12), similar to those reported by Singh et al. for Au(111), Au(100), and Au(211) surfaces [70]. The H-assisted C-H activation pathway, suggested by Ojeda and Iglesia, involved the activation barrier that was 0.1 eV higher than those involved in the unassisted pathway. The authors suggested that the proposed mechanism agrees well with the measured KIE values for both C-H and O-H substitutions, where the normal KIE

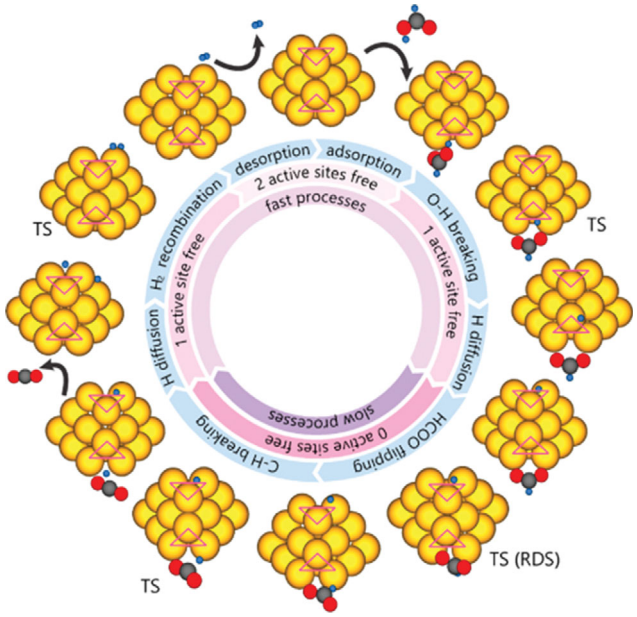

Fig. 12. Proposed reaction mechanism for HCOOH dehydrogenation on Au_{18} clusters (Reproduced with permission from Ref. [71], Copyright 2019, American Chemical Society).

for HCOOD was explained by the thermodynamic isotope effects. These calculations also suggested that each discrete Au_{18} cluster catalyzes decomposition of one HCOOH molecule at a time, explaining the exclusive formation of HD from HCOOD and DCOOH isotopes. These computational models resulted in the reaction order of HCOOH (0.72) that was close to that for Au/SiC (0.95) [70], but inconsistent with the zero-order kinetics observed on Au/Al_2O_3 [43] and Au/SiO_2 [69]. These results, in turn, demonstrate the complexity and ongoing controversy of HCOOH dehydrogenation routes on small Au nanoparticles, specifically those that are invisible in electron microscopes but dominantly contribute to the overall turnover rates.

5. Comparisons of Transition Metal Catalysts

Previous works discussed thus far for Cu, Pt, Pd, and Au catalysts demonstrate the complexity of HCOOH decomposition routes on transition metal surfaces, despite the seemingly "simple" structure of HCOOH. Specifically, controversies continue regarding the types of reactive intermediates and the kinetic consequences of elementary steps, which may depend on the nature of metal surfaces and exposed facets, but also on the surface coverage of co-adsorbates. As the relevant surface coverage of bound intermediates varies with the reaction conditions (which can have an impact on reaction pathways and reactivity/selectivity of metal surfaces), it is difficult to rigorously compare different catalysts without understanding the reaction pathways relevant at specific conditions. Regardless, general trends of catalytic performance of transition metal catalysts for HCOOH dehydrogenation catalysis have been suggested by several research groups based on theoretical calculations [23,42] and experimental observations [37].

Herron and co-workers provided a comprehensive theoretical study of HCOOH decomposition pathways on model (111) and (100) facets of fcc metals (Au, Ag, Cu, Pt, Pd, Ni, Ir, and Rh) and (0001) facets of hcp (Co, Os, Ru, and Re) metals based on DFT calculations (PW91 functionals) [42]. Based on the energy of intermediates involved in COOH*- and $HCOO_B$*-mediated pathways (Fig. 13), they determined that the most optimal catalysts are Pt(111), Pd(111), Pd(100), Cu(111), and Cu(100), which balanced the requirements for the two dehydrogenation steps. They also analyzed the CO_2/CO selectivity by investigating the stability of COOH* intermediates and its decomposition to CO_2 vs. CO products, which led to the conclusion that a significant CO formation is expected on Pt(100), Pd(100), Rh(100), and Ir(100) surfaces. These analyses, in turn, proposed Cu as the most active, selective, and economic metal for HCOOH dehydrogenation. Yet, these analyses were based solely on thermodynamics, and the results may vary upon the consideration of kinetics and the realistic surface coverages of intermediates.

Yoo et al. [23] performed theoretical analyses of HCOOH decomposition pathways on stepped (Ag(211), Cu(211), Pd(211), Pt(211), and Rh(211)) and closely packed surfaces (Cu(111), Pd(111), and Pt(111)) to provide catalytic descriptors that determine their reactivity and selectivity (between dehydrogenation and dehydration pathways). In doing so, they showed that both dehydrogenation

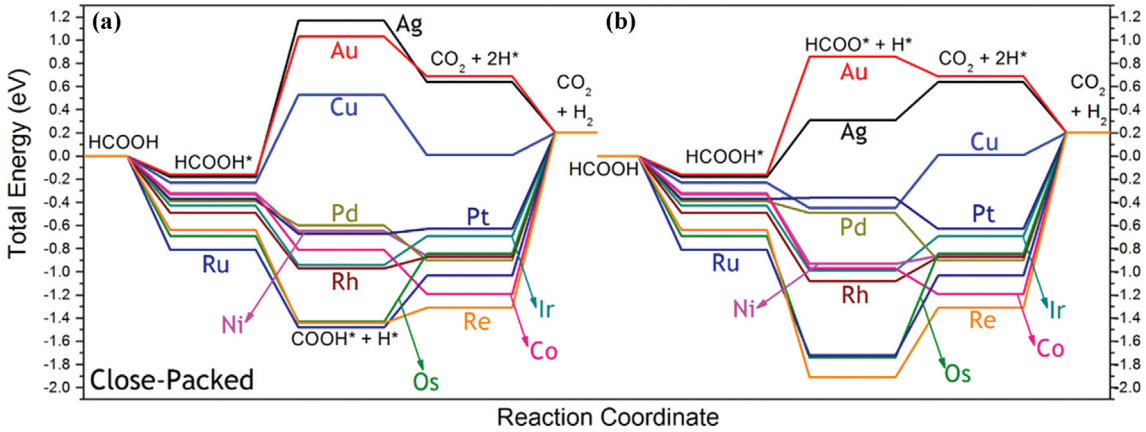

Fig. 13. DFT-derived energy (in eV; without any corrections) of intermediates involved in HCOOH dehydrogenation via (a) carboxyl (COOH*) and (b) formate (HCOO*) pathways on fcc(111) and hcp(0001) facets (Reproduced with permission from Ref. [42], Copyright 2014, American Chemical Society).

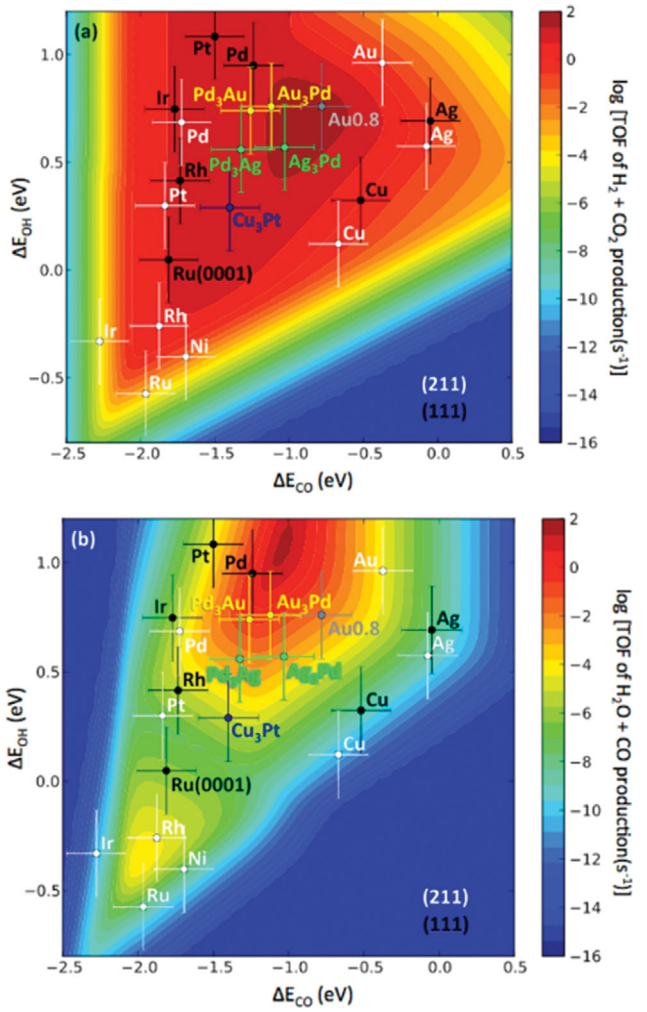

Fig. 14. Theoretical activity volcano plots for (a) H_2+CO_2 production and (b) H_2O+CO production turnover frequency (TOFs) from HCOOH decomposition on transition metal catalysts. The logarithms of the turnover frequency (TOFs) were plotted as functions of CO and OH adsorption energy (ΔE_{CO} and ΔE_{OH}), taken relative to electronic energy of CO, H_2, and H_2O in the gas phase. The error bars indicate an estimated error of 0.2 eV for ΔE_{CO} and ΔE_{OH}, compared to their experimental values (Reproduced with permission from Ref. [23], Copyright 2014, American Chemical Society).

and dehydration reactivity depend on CO and OH binding energies, which act as the reactivity descriptors for transition metal surfaces (Fig. 14). Theory-derived turnover frequency (TOFs) for HCOOH dehydrogenation showed volcano-shaped relations when plotted against OH and CO binding energy (Fig. 14(a)); the precious metals (Pd, Pt, Ir, Ru, and Rh) showed high rates, as expected from previous experiments [37]. Interestingly, they found that the stepped sites of binary alloys, such as Au_3Pd and Ag_3Pd, present at the top of the activity volcano, consistent with the recent experimental results that showed high reactivity of these bimetallic systems [65-67]. They also used the analogous analyses to understand HCOOH dehydration rates (that form CO/H_2O), which were several orders of magnitude lower than the desired HCOOH dehydrogenation routes on all transition metal surfaces examined in their work (Fig. 14(b)). The metals that were very active for HCOOH dehydrogenation (e.g., Pd-Au and Pd-Ag binary alloys) are expected to be also active for HCOOH dehydration catalysis, forming a considerable amount of CO at relevant conditions (>100 ppm CO). Alternatively, the authors suggested Cu_3Pt alloy catalysts as a promising material for selective HCOOH dehydrogenation catalysis, which are as active as the previously identified precious metals but with a minimal amount of CO formation.

Table 2 summarizes the catalytic performance of different transition metals discussed thus far; we tried to only include the rate data reported per surface metal atoms (turnover frequency). These results provide the general trend of HCOOH dehydrogenation rates across different metals, although careful consideration must be made in compartmenting experiments performed at different conditions and HCOOH concentrations. In general, HCOOH dehydrogenation activity follows the trend of Cu<<Pt<Au~Pd<PdNi~PdAu, the trend that is very similar to those expected from the theoretical work by Yoo et al. (Fig. 13). However, the reactivity of transition metals depends sensitively on their particle size, especially Pt and Au, which showed nearly an order-of magnitude range of turnover rate even at a given condition (Table 2). The type of supports can also influence rates but moreso selectivity, as shown for Au nanoparticles supported on different supports that show a wide range of CO_2 selectivity (10-100%; Table 2, albeit measured at different conversions). These data teach us the importance of understanding the fundamentals of reaction mechanisms in order to provide fair comparisons among different transition metals and to rationally design catalysts with improved catalytic performance.

SUMMARY AND FUTURE PERSPECTIVES

HCOOH has emerged as a potential liquid-phase H_2 carrier to store and release H_2 on demand. Its industrial application requires development of an efficient catalytic system to dehydrogenate HCOOH at low temperatures without forming any CO co-products that may significantly inhibit the use of H_2 product stream in fuel cell applications. In this review, we summarized the current understanding of HCOOH decomposition routes on transition metal surfaces to facilitate such routes in utilizing HCOOH as a potential H_2 carrier. We focused on the surface chemistry on various metal surfaces, including Cu, Pt, Pd, and Au, with a goal providing insights on the catalytic properties that influence reactivity and selectivity. We laid out the current debate in literature and the factors that may significantly influence the reaction rates and selectivity, including surface structures, particle size effects, and solvent effects. The general trends of the reactivity of transition metals are described, which follow the order of Cu<<Pt<Au~Pd<PdNi~PdAu, although the specific performance may also depend on their particle size, identity of support, and operating condition.

Transition metal catalysts are often prepared as metal nanoparticles supported on high surface area metal oxides, such as TiO_2, Al_2O_3, SiO_2, and MgO. Although this article did not discuss much on the support effects, these metal oxides can have reactivity for HCOOH decomposition reactions, especially at higher temperatures. For details of HCOOH decomposition routes on metal oxides,

Table 2. A summary of catalytic performance of different transition metals

Metal	Catalyst	T (K)	Reaction phase	HCOOH concentration (kPa or M)[a]	Conversion (%)	CO_2 selectivity	TOF (s^{-1})[e]	Ref.
Cu	Cu powder	470	Gas	0.1-20	≤10	100	0.16	[34]
	Cu/SiO_2	450	Gas	0.1-20	≤10	100	0.16	
	Cu/SiO_2	473	Gas	3.5	≤10	100	0.57	[35]
Pt	Pt/Al_2O_3	353	Gas	4	≤10	100	0.014-0.084[f]	[43]
	Pt/C	373	Gas	1-5	≤10	≥98.8	0.15	[47]
		378	Gas	1-5	≤10	≥98.8	0.19	
Pd	Pd Powder	523	Gas	0.2	≤2	N/A	16	[37]
	Pd/MnOx	348	Liquid	2 M (+16 M HCOONa)	0-100	100	0.13	[72]
	$Pd/CN_{0.25}$	298	Liquid	1 M	0-97.5	100	1.5	[73]
Au	Au/Al_2O_3	353	Gas	2	≤10	100	0.045-0.51[f]	[43]
	Au/ZrO_2	353	Liquid	10.5	0-95	100	0.18	[74]
	Au/SiO_2	473	Gas	7	63	100	2.0	[69]
	Au/C	473			25	97	0.30	
	Au/CeO_2	473			18	100	0.08	
	Au/Al_2O_3	473			N/A	10	0.005	
	Au/ZSM-5	473			N/A	10	0.03	
Pd_8Au_2	Pd_8Au_2/C_3N_4	303	Liquid	1.5 M (+0.5 M HCOONa)	0-100	100	0.13	[75]
PdNi	PdNi/C	298	Liquid	1 M (+1 M HCOONa)	0-100	100	0.15	[76]

[a]HCOOH concentrations are given as pressures (kPa) for gas-phase experiments and molar concentrations (M) for liquid phase experiments.
[e]Turn-over frequency (TOF) is calculated defined as the molecule of CO_2/H_2 formed per surface metal atom per second.
[f]The TOF range reflects the difference in Pt (1-8 nm) and Au (3-4 nm) particle sizes varied by the pretreatment conditions.

readers are referred to previous review articles by Mars et al. [77] and Trillo et al. [78]. In general, MgO and ZnO are considered as HCOOH dehydrogenation catalysts [79], while TiO_2, SiO_2, and Al_2O_3 are known as dehydration catalysts [80,81]; yet, even on MgO and ZnO catalysts, dehydration products (CO/H_2O) are detected along with dehydrogenation products (CO_2/H_2), which may come directly from HCOOH decomposition or via reverse water-gas shift reaction ($CO_2+H_2 \rightarrow CO+H_2O$) [82]. A careful selection of supports is thus needed to prevent the involvement of undesired CO formation during HCOOH reactions.

Lastly, this review article focused on the dehydrogenation part of the hydrogenation-dehydrogenation cycle in using HCOOH as a potential H_2 carrier. The hydrogenation part of the cycle ($CO_2(g)+H_2(g) \rightarrow HCOOH(g)$) is, in fact, more challenging with unfavorable thermodynamics ($\Delta G_{298\,K}$=+48.4 kJ mol^{-1}), requiring efforts in developing reaction systems to store H_2 with reactions with CO_2; such routes are also critical to close the CO_2 cycle to minimize CO_2 emissions to atmosphere. The recent efforts to develop catalysts for this hydrogenation step are summarized in the review articles provided by Álvarez et al. [83], Zhao et al. [84], Whang et al. [85], Sun et al. [86], Yan et al. [87], Onishi et al. [88] and Chen et al. [89] in their respective articles.

ACKNOWLEDGEMENTS

We thank Ting Lin (U. of Minnesota), Unai De La Torre (U. of the Basque Country, Spain), and Emily Volk (Colorado School of Mines) for providing a careful proofreading of the manuscript. We also acknowledge the financial support from Colorado School of Mines (the startup funding and Mines Summer Undergraduate Research Fellowship).

REFERENCES

1. R. Borup, T. Krause and J. Brouwer, *Electrochem. Soc.*, **30**, 79 (2021).
2. H. Kawanami, Y. Himeda and G. Laurenczy, *Adv. Inorg. Chem.*, **70**, 395 (2017).
3. W. L. Mao and H. K. Mao, *Proc. Natl. Acad. Sci. U. S. A.*, **101**, 708 (2004).
4. Y. J. Colón, D. Fairen-Jimenez, C. E. Wilmer and R. Q. Snurr, *J. Phys. Chem.*, **118**, 5383 (2014).
5. M. P. Suh, H. J. Park, T. K. Prasad and D. W. Lim, *Chem. Rev.*, **112**,

782 (2012).
6. L. J. Murray, M. Dincă and J. R. Long, *Chem. Soc. Rev.*, **38**, 1294 (2009).
7. W. X. Lim, A. W. Thornton, A. J. Hill, B. J. Cox, J. M. Hill and M. R. Hill, *Langmuir*, **29**, 8524 (2013).
8. B. Viswanathan, *Energy Sources*, 185 (2017).
9. J. Andersson and S. Grönkvist, *Int. J. Hydrogen Energy*, **44**, 11901 (2019).
10. S. Kim, J. Chen, T. Cheng, A. Gindulyte, J. He, S. He, Q. Li, B. A. Shoemaker, P. A. Thiessen, B. Yu, L. Zaslavsky, J. Zhang and E. E. Bolton, *PubChem*, **49**, 971 (2022).
11. J. Guo, C. K. Yin, D. L. Zhong, Y. L. Wang, T. Qi, G. H. Liu, L. T. Shen, Q. S. Zhou, Z. H. Peng, H. Yao and Z. B. Li, *Chem. Sus. Chem.*, **14**, 2655 (2021).
12. J. Kothandaraman, S. Kar, R. Sen, A. Goeppert, G. A. Olah and G. K. S. Prakash, *J. Am. Chem. Soc.*, **139**, 2549 (2017).
13. M. Aziz, T. Oda and T. Kashiwagi, *Energy Procedia*, **158**, 4086 (2019).
14. M. Aziz, A. T. Wijayanta and A. B. D. Nandiyanto, *Energies*, **13**, 3062 (2020).
15. F. Sanchez, D. Motta, A. Roldan, C. Hammond, A. Villa and N. Dimitratos, *Topics Catal.*, **61**, 254 (2018).
16. Y. Ahn, J. Byun, D. Kim, B. S. Kim, C. S. Lee and J. Han, *Green Chem.*, **21**, 3442 (2019).
17. L. Vermaak, H. W. J. P. Neomagus and D. G. Bessarabov, *Membranes*, **11**, 670 (2021).
18. N. Hoshi, K. Kida, M. Nakamura, M. Nakada and K. Osada, *J. Phys. Chem. B*, **110**, 12480 (2006).
19. S. Hu, F. Munoz, J. Noborikawa, J. Haan, L. Scudiero and S. Ha, *Appl. Catal. B: Environ.*, **180**, 758 (2016).
20. S. Hu, L. Scudiero and S. Ha, *Electrochem. Commun.*, **38**, 107 (2014).
21. J. Yang, S. Yang, Y. Chung and Y. Kwon, *Korean J. Chem. Eng.*, **37**, 176 (2020).
22. A. Rahbari, M. Ramdin, L. J. P. van de Broeke and T. J. H. Vlugt, *Ind. Eng. Chem. Res.*, **57**, 10663 (2018).
23. J. S. Yoo, F. Abild-Pedersen, J. K. Nørskov and F. Studt, *ACS Catal.*, **4**, 1226 (2014).
24. M. Bowker, E. Rowbotham, F. M. Leibsle and S. Haq, *Surf. Sci.*, **349**, 97 (1996).
25. M. Bowker, S. Haq, R. Holroyd, P. M. Parlett, S. Poulston and N. Richardson, *J. Chem. Soc., Faraday Trans.*, **92**, 4683 (1996).
26. Y. Shiozawa, T. Koitaya, K. Mukai, S. Yoshimoto and J. Yoshinobu, *J. Chem. Phys.*, **143**, 234707 (2015).
27. D. H. S. Ying and R. J. Madix, *J. Catal.*, **61**, 48 (1980).
28. B. E. Hayden, K. Prince, D. P. Woodruff and A. M. Bradshaw, *Surf. Sci.*, **133**, 589 (1983).
29. L. H. Dubois, T. H. Ellis, B. R. Zegarski and S. D. Kevan, *Surf. Sci.*, **172**, 385 (1986).
30. R. J. Madix and S. G. Telford, *Surf. Sci.*, **277**, 246 (1992).
31. Y. Yao and F. Zaera, *Surf. Sci.*, **646**, 37 (2016).
32. S. Li, J. Scaranto and M. Mavrikakis, *Topics Catal.*, **59**, 1580 (2016).
33. B. W. J. Chen and M. Mavrikakis, *ACS Catal.*, **10**, 10812 (2020).
34. E. Iglesia and M. Boudart, *J. Phys. Chem.*, **90**, 5272 (1986).
35. T. C. Lin, U. D. L. Torre, A. Hejazi, S. Kwon and E. Iglesia, *J. Catal.*, **404**, 814 (2021).
36. E. Iglesia and M. Boudart, *J. Catal.*, **81**, 214 (1983).
37. Y. Tang, C. A. Roberts, R. T. Perkins and I. E. Wachs, *Surf. Sci.*, **650**, 103 (2016).
38. M. B. Jensen, U. Myler and P. A. Thiel, *Surf. Sci. Lett.*, **290**, L655 (1993).
39. N. R. Avery, *Appl. Surf. Sci.*, **11**, 774 (1982).
40. N. Abbas and R. J. Madix, *Appl. Surf. Sci.*, **16**, 424 (1983).
41. J. Scaranto and M. Mavrikakis, *Surf. Sci.*, **648**, 201 (2016).
42. J. A. Herron, J. Scaranto, P. Ferrin, S. Li and M. Mavrikakis, *ACS Catal.*, **4**, 4434 (2014).
43. M. Ojeda and E. Iglesia, *Angew. Chem. Int. Ed.*, **48**, 4800 (2009).
44. M. R. Columbia and P. A. Thiel, *Surf. Sci.*, **235**, 53 (1990).
45. E. Becker, M. Skoglundh, M. Andersson and A. L. Spetz, IEEE Sensors (2007).
46. M. R. Columbia, A. M. Crabtree and P. A. Thiel, *J. Electroanal. Chem.*, **345**, 93 (1993).
47. S. Bhandari, S. Rangarajan, C. T. Maravelias, J. A. Dumesic and M. Mavrikakis, *ACS Catal.*, **10**, 4112 (2020).
48. Y. Kim, S. Kim, H. C. Ham and D. H. Kim, *J. Catal.*, **389**, 506 (2020).
49. J. Li, W. Chen, H. Zhao, X. Zheng, L. Wu, H. Pan, J. Zhu, Y. Chen and J. Lu, *J. Catal.*, **352**, 371 (2017).
50. S. Jones, A. Kolpin and S. C. E. Tsang, *Catal., Struct. React.*, **1**, 19 (2014).
51. Y. Kim, H. Lee, S. Yang, J. Lee, H. Kim, S. Hwang, S. W. Jeon and D. H. Kim, *J. Catal.*, **404**, 324 (2021).
52. C. Hu, J. K. Pulleri, S. W. Ting and K. Y. Chan, *Int. J. Hydrogen Energy*, **39**, 381 (2014).
53. A. Bulut, M. Yurderi, Y. Karatas, M. Zahmakiran, H. Kivrak, M. Gulcan and M. Kaya, *Appl. Catal. B: Environ.*, **164**, 324 (2015).
54. S. W. Jorgensen and R. J. Madix, *J. Am. Chem. Soc.*, **110**, 397 (1988).
55. J. L. Davis and M. A. Barteau, *Surf. Sci.*, **256**, 50 (1991).
56. J. Scaranto and M. Mavrikakis, *Surf. Sci.*, **650**, 111 (2016).
57. R. Zhang, H. Liu, B. Wang and L. Ling, *J. Phys. Chem. C*, **116**, 22266 (2012).
58. S. Li, S. Rangarajan, J. Scaranto and M. Mavrikakis, *Surf. Sci.*, **709**, 121846 (2021).
59. Y. Wang, Y. Qi and D. Zhang, *Comput. Theor. Chem.*, **1049**, 51 (2014).
60. K. Jiang, K. Xu, S. Zou and W. B. Cai, *J. Am. Chem. Soc.*, **136**, 4861 (2014).
61. Q. L. Zhu, N. Tsumori and Q. Xu, *J. Am. Chem. Soc.*, **137**, 11743 (2015).
62. F. Z. Song, Q. L. Zhu, N. Tsumori and Q. Xu, *ACS Catal.*, **5**, 5141 (2015).
63. D. M. Ruthven and R. S. Upadhye, *J. Catal.*, **21**, 39 (1971).
64. Y. Kim and D. H. Kim, *Appl. Catal. B: Environ.*, **244**, 684 (2019).
65. X. Zhou, Y. Huang, W. Xing, C. Liu, J. Liao and T. Lu, *Chem. Commun.*, **30**, 3540 (2008).
66. Y. Huang, X. Zhou, M. Yin, C. Liu and W. Xing, *Chem. Mater.*, **22**, 5122 (2010).
67. S. Zhang, Ö. Metin, D. Su and S. Sun, *Angew. Chem. Int. Ed.*, **52**, 3681 (2013).
68. K. Mandal, D. Bhattacharjee and S. Dasgupta, *Int. J. Hydrogen Energy*, **40**, 4786 (2015).
69. A. Gazsi, T. Bánsági and F. Solymosi, *J. Phys. Chem. C*, **115**, 15459 (2011).
70. S. Singh, S. Li, R. Carrasquillo-Flores, A. C. Alba-Rubio, J. A. Dumesic and M. Mavrikakis, *AIChE J.*, **60**, 1303 (2014).

71. B. W. J. Chen, M. Stamatakis and M. Mavrikakis, *ACS Catal.*, **9**, 9446 (2019).
72. Q. F. Deng, Z. F. Zhang, F. J. Cui and L. H. Jia, *Int. J. Hydrogen Energy*, **42**, 14865 (2017).
73. Q. Y. Bi, J. D. Lin, Y. M. Liu, H. Y. He, F. Q. Huang and Y. Cao, *Angew. Chem. Int. Ed.*, **55**, 11849 (2016).
74. Q. Y. Bi, J. D. Lin, Y. M. Liu, H. Y. He, F. Q. Huang and Y. Cao, *J. Power Sources*, **328**, 463 (2016).
75. L. X. Xu, F. Yao, J. L. Luo, C. Wan, M. F. Ye, P. Cui and Y. An, *RSC Adv.*, **7**, 4746 (2017).
76. Y. Qin, J. Wang, F. Meng, L. Wang and X. Zhang, *Chem. Commun.*, **49**, 10028 (2013).
77. P. Mars, J. J. F. Scholten and P. Zwietering, *Adv. Catal.*, **14**, 35 (1963).
78. J. M. Trillo, G. Munuera and J. M. Criado, *Catal. Rev.*, **7**, 51 (1972).
79. Y. Noto, K. Fukuda, T. Onishi and K. Tamaru, *Trans. Faraday Soc.*, **63**, 3081 (1967).
80. K. Fukuda, Y. Noto, T. Onishi and K. Tamaru, *Trans. Faraday Soc.*, **63**, 3072 (1967).
81. S. Kwon, T. C. Lin and E. Iglesia, *J. Phys. Chem. C*, **124**, 20161 (2020).
82. S. Rajadurai, *Catal. Rev.*, **36**, 385 (1994).
83. A. Álvarez, A. Bansode, A. Urakawa, A. V. Bavykina, T. A. Wezendonk, M. Makkee, J. Gascon and F. Kapteijn, *Chem. Rev.*, **117**, 9804 (2017).
84. G. Zhao, X. Huang, X. Wang and X. Wang, *J. Mater. Chem. A*, **5**, 21625 (2017).
85. H. S. Whang, J. Lim, M. S. Choi, J. Lee and H. Lee, *BMC Chem. Eng.*, **1**, 9 (2019).
86. R. Sun, Y. Liao, S. T. Bai, M. Zheng, C. Zhou, T. Zhang and B. F. Sels, *Energy Environ. Sci.*, **14**, 1247 (2021).
87. N. Yan and K. Philippot, *Curr. Opin. Chem. Eng.*, **20**, 86 (2018).
88. N. Onishi, M. Iguchi, X. Yang, R. Kanega, H. Kawanami, Q. Xu and Y. Himeda, *Adv. Energy Mater.*, **9**, 1801275 (2019).
89. X. Chen, Y. Liu and J. Wu, *Mol. Catal.*, **483**, 110716 (2020).